ACS NANO

www.acsnano.org

Fiber-Optic Quantum Dots Sensor for Dynamic and Quantitative Thermal Monitoring of Spheroids toward Single-Cellular Resolution

Dongliang Hu,◆ Jialu Zhang,◆ Yang Zong,◆ Minjie Xi, Luxi Hu, Kaijie Zhu, Zhipeng Zhu, Liang Xu, Yongfeng Mei, Xuanyong Liu,* Jizhai Cui,* Kewang Nan,* and Xiaoqi Hou*

Cite This: https://doi.org/10.1021/acsnano.6c06731

Read Online

ACCESS | Metrics & More | Article Recommendations | Supporting Information

ABSTRACT: **Accurate monitoring of thermal dynamics at the single-cellular scale is crucial for elucidating metabolism, signaling pathways and disease mechanisms, yet remains hampered by the limited stability and spatiotemporal resolution of current sensors. Here, we report a fiber-optic quantum dots sensor (FOQDS), which is based on a tapered fiber optic tip functionalized with CdSe/CdS/ZnS QDs and encapsulated by a dense Al_2O_3 layer to ensure exceptional long-term stability. FOQDS features a linear thermal response with high sensitivity (145 pm/°C), a temporal resolution of <10 μs, with the potential to achieve single-cellular-scale spatial precision. This performance enables quantitative and real-time monitoring of pharmacologically induced thermal fluctuations within living three-dimensional glioblastoma spheroids. This work provides a stable and minimally invasive platform for monitoring cellular thermogenesis in physiologically relevant microenvironments, with promising prospects in applications of fundamental biology and precision therapeutics.**

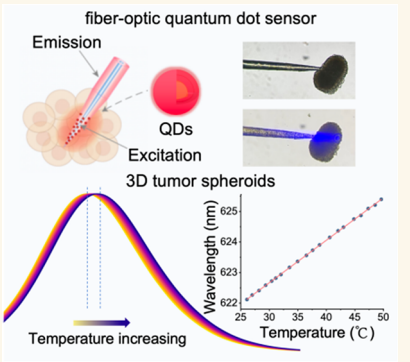

KEYWORDS: *fiber-optic sensor, colloidal quantum dots, temperature sensing, single-cell resolution, thermal dynamics*

INTRODUCTION

Temperature is a fundamental physiological parameter that governs many biochemical reactions, metabolic activities, and signaling pathways within a living cell.[1,2] It acts not only as a passive indicator but also as an active regulator of cellular homeostasis, proliferation, and even apoptosis.[3−5] Recently, measurements at the single-cell level have been used to reveal cellular temperature gradients and organelle-related thermogenesis,[6] monitor thermal signaling during neuronal differentiation,[7] and track dynamic thermal responses to metabolic perturbations in tumor cells.[8] Consequently, the ability to monitor thermal dynamics at the cellular scale with high spatial and temporal resolution holds the potential to provide profound insights into cellular physiology, disease mechanisms, and the efficacy of therapeutic interventions.[8−12]

Despite the critical importance of cellular temperature monitoring, achieving minimally invasive, quantitative, and real-time measurement at the single-cellular scale remains a formidable challenge. Over the past decades, conventional temperature measurement techniques, such as thermocouples,[13,14] thermistors,[15] and infrared thermography,[16] have been widely used for macroscopic-scale detection. However, their relatively large sensor size and insufficient spatial resolution make them unsuitable for cellular-scale probing. Furthermore, electronic temperature sensors,[17−19] although capable of certain real-time monitoring functions, are limited by susceptibility to electromagnetic interference, challenges in miniaturization and potential electrical safety hazards, restricting their broader biomedical application. In recent years, a suite of nanoscale thermometers primarily based on fluorescent materials such as fluorescent proteins, organic dyes and lanthanide-doped nanoparticles, has attracted significant attention due to its capabilities for high sensitivity, nonionizing radiation, and low invasiveness.[20−25] While these nanothermometers have demonstrated great potential for temperature monitoring and imaging, they often suffer from inherent limitations, including photobleaching, broad emission spectra,

Received: April 9, 2026
Revised: June 19, 2026
Accepted: June 22, 2026

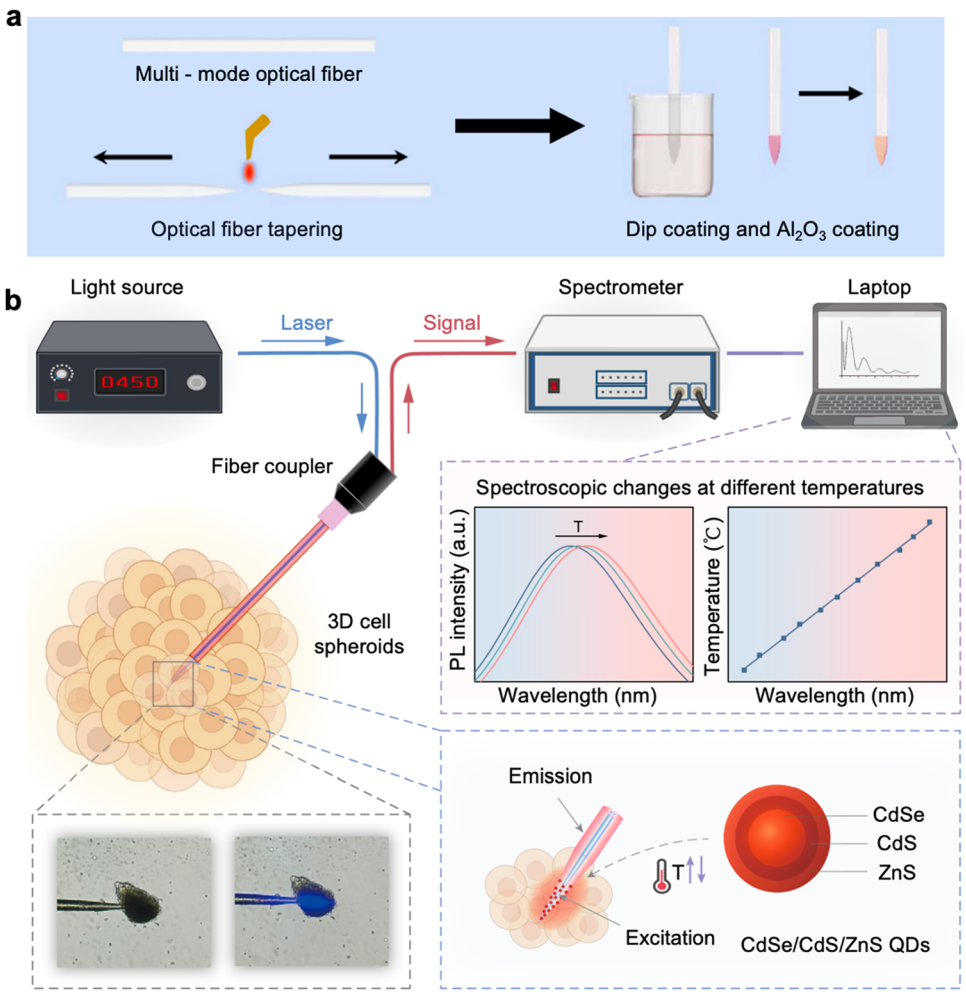

Figure 1. Dual-functional-layer tapered fiber-optic temperature sensor based on QDs. (a) Fabrication process of the tapered fiber with a dual-functional layer. (b) Schematic illustration of the temperature sensing system employing fluorescence detection.

and environmental sensitivity. To achieve adequate signal-to-noise ratios, they often require integration times of several seconds, imposing a critical constraint on temporal resolution.[25] Such a limitation is particularly problematic for thermal monitoring in three-dimensional (3D) spheroids, where rapid thermal transients associated with metabolism or signaling may unfold on the time scale of seconds or less, and would likely be averaged out by conventional approaches that require long integration times. Moreover, these optical methods are fundamentally limited by light scattering when applied to 3D tissue models leading to signal averaging and loss of single-cellular resolution. These factors complicate signal discrimination from autofluorescence and lead to measurement inaccuracies.

With the rapid advancement of fluorescent nanomaterials, colloidal quantum dots (QDs) have emerged as a promising alternative[26−31] due to their exceptional photostability, high photoluminescence quantum yield (PL QY), outstanding solution processability, and size-tunable optical properties. It is particularly worth noting that QDs exhibit high sensitivity and reversibility to temperature variations, which typically display as a temperature-dependent shift in their fluorescence peak or intensity.[32−35] This phenomenon endows them with an outstanding potential for precise temperature detection and real-time thermodynamic monitoring. However, a critical gap persists between the demonstration of QDs as nanothermometers in solution and their practical applications in microscopic and confined biological systems. Most existing platforms lack the capability for continuous and long-term monitoring within a stable and minimally invasive microenvironment, which is crucial for studying dynamic biological processes. Therefore, the integration of sensing materials with suitable transduction platforms is important. Optical fibers present a unique solution to this integration challenge for biological sensing.[36,37] Their miniaturized, flexible form factor, and efficient light delivery/collection capabilities enable access to confined microscopic sites, such as within single cells or deep inside living tissues, which are inaccessible to conventional spectroscopic methods. Functionalizing the fiber with sensing materials allows for precise in situ and single-spot detection.[38−40] The combination of the superior optical properties and solution processability of QDs with the minimally invasive platform of micro-optical fibers is therefore envisioned as a highly promising route for developing novel temperature monitoring technologies toward the single-cell level.

However, there are still huge obstacles for transforming this conceptual promise into a reliable tool applicable to complex biological environments. The limited long-term stability of QDs against photo-oxidation and the unpredictable influence of the local biochemical environment on their optical properties have constrained existing sensors.[25,41,42] Further-

https://doi.org/10.1021/acsnano.6c06731
ACS Nano XXXX, XXX, XXX−XXX

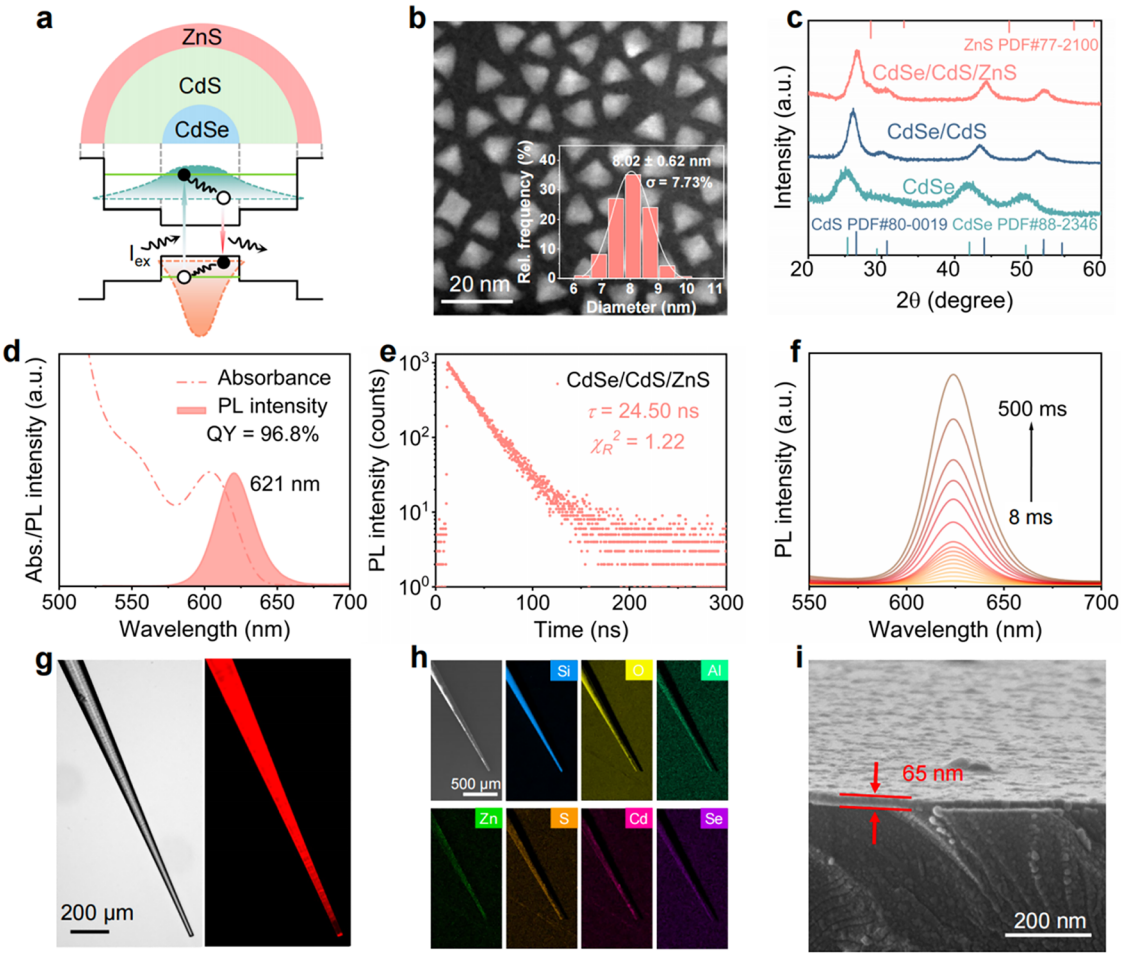

Figure 2. Synthesis and Characterization of QDs and the fiber-optic sensor. (a) Energy-level structure of CdSe/CdS/ZnS QDs. (b) HAADF-STEM image of the QDs. (c) XRD patterns of CdSe, CdSe/CdS and CdSe/CdS/ZnS QDs. (d) Normalized PL spectrum (solid line) and absorption spectrum (dotted line) of the QDs. (e) Transient PL spectra of the QDs. (f) PL spectra under different integration times in the fiber-optic sensing system. (g) Fluorescence microscopy image of the tapered fiber tip. (h) EDS elemental mapping images of the dual-functional-layer-coated tapered fiber, showing the distribution of key components (Si, O, Al, Zn, S, Cd, Se). (i) Cross-sectional SEM image of the QDs-functionalized fiber-optic sensor.

more, capturing rapid, metabolism-driven thermal transients within dense 3D tissue microenvironments with minimal invasiveness imposes simultaneous demands for high temporal resolution and sensitivity as well as single-cellular spatial resolution. This requires extremely miniaturized tools capable of precise and single-spot measurement over extended periods without perturbing the native microstructure. Consequently, a platform that integrates long-term stability, spatiotemporal resolution, and minimal invasiveness for thermal monitoring in living 3D systems remains an unmet need.

In this work, we developed a sensitive and stable fiber-optic QDs sensor (FOQDS) integrated with a dual-function layer for dynamic and quantitative monitoring of thermal fluctuations toward the single-cellular scale. The CdSe/CdS/ZnS core/shell/shell QDs with outstanding optical property were elected as an ideal luminophore for sensing temperature and encapsulated it with a conformal dense alumina (Al_2O_3) layer via atomic layer deposition (ALD) to solve the stability bottleneck, creating a chemically inert shield. This film was functionalized on a tapered fiber tip (<10 μm), enabling minimally invasive insertion into 3D spheroids to overcome the spatial-access limitation. FOQDS achieved a sensitivity of 145 pm/°C and a temporal resolution of <10 μs. Furthermore, we demonstrated its capability for real-time and quantitative temperature monitoring of living three-dimensional glioblastoma spheroids in situ under different pharmacological interventions, revealing metabolically driven thermal fluctuations inaccessible to conventional bulk fluorescence imaging.

RESULTS AND DISCUSSION

Design and Fabrication of FOQDS

As illustrated in Figure 1a, FOQDS was composed of a flexible optical fiber with a tapered tip that is designed to be inserted into cell spheroids. On the distal tip of the optical fiber, a uniform QDs film was carried on the tapered fiber surface using a straightforward solution-based coating process, followed by the deposition of a conformal and dense Al_2O_3 thin film via ALD to encapsulate the sensing probes. Figure 1b shows the schematic of the designed optical fiber sensing system. A flexible Y-shaped optical fiber was adopted to transmit the laser source to excite the QDs sensing films and detected the reflected fluorescence signal continuously via a portable spectrometer for dynamic temperature monitoring. The optical fiber was tapered to a conical tip with a diameter of less than 10 μm to achieve low-loss optical transmission (<0.05

https://doi.org/10.1021/acsnano.6c06731
ACS Nano XXXX, XXX, XXX−XXX

dB/cm) and holds promise for single-cellular spatial resolution for temperature detection. The spectrometer was connected to a computer for signal processing and visualization.

The sensor probe was fabricated by flame-heated taper drawing of a standard step-index multimode fiber (core/cladding diameter: 105/125 μm). This tapered geometry confers several critical advantages for sensing. The micron-scale tip diameter enabled optical access to microscopic regions, while the tapering process concentrates the guided light, resulting in a high energy density at the tip for efficient excitation. Furthermore, the structural modification promoted the leakage of excitation light from the tapered region to interact with the QDs while enhancing the recapture of fluorescence back into the fiber mode, thus contributing to the high temporal resolution of the system. These beneficial optical characteristics, which underpin the sensor's performance, were corroborated by simulations of the light intensity distribution along the tapered fiber (Figure S1).

Although both the luminescence intensity and peak shift of the QDs can be used to obtain temperature information, the former is compromised by extrinsic factors such as optical power drift and coupling inefficiencies. Our strategy circumvented these issues by leveraging the physical redshift in the QD emission peak, which was primarily governed by the temperature-induced modulation of the semiconductor bandgap energy. The dominant mechanisms underlying this modulation were the intricate interactions between charge carriers and lattice vibrations,[34,43] complemented by effects arising from thermal expansion of the crystal lattice.[32] As this response was an intrinsic material property, it provided an absolute measurement that was invariant to excitation power or other environmental factors. This attribute offered significant advantages, including calibration-free operation, universal applicability, and an inherent compatibility with batch fabrication.

Characterization of QDs and FOQDS

In fluorescence-based thermometry, surface and lattice defects act as nonradiative recombination centers that effectively quench the emission intensity and cause signal instability, thereby compromising measurement accuracy.[32,34,43] Moreover, to compensate for the poor signal-to-noise ratio resulting from the low brightness, increased integration times are often required, which would harm temporal resolution. Therefore, the development of high-brightness nanothermometers with superior optical stability is critical for achieving reliable, real-time thermal sensing. The high-quality CdSe/CdS/ZnS core/shell/shell QDs with monoexponential PL decay dynamics and near-unity PL QY were constructed in the present study. Figure 2a illustrated the energy band alignment of the QD, designed with a structure confining the band-edge hole wavefunction mainly within the CdSe core and delocalizing the band-edge electron wavefunction over the CdSe/CdS region. The outer ZnS shell with large bandgap served as an effective barrier that isolated the electron wavefunction from the environment, thus substantially enhancing photostability. To achieve nearly ideal emission properties, we developed a controlled synthesis of CdSe/CdS/ZnS QDs, as detailed in Methods. Briefly, CdSe core QDs with an average diameter of 3.2 nm were first synthesized, followed by the successive epitaxial growth of approximately 7 monolayers of CdS shell and 1.5 monolayers of ZnS shell to ensure effective exciton confinement and surface passivation (Figure S2). As shown by High-angle annular dark-field scanning transmission electron microscopy (HAADF-STEM) images in Figure 2b, the QDs exhibited nearly monodisperse hexahedral shapes with an average size of 8.02 $\pm$ 0.62 nm. X-ray diffraction (XRD) analysis confirmed single-crystalline zinc-blende structure of the QDs (Figure 2c). The absorption and steady-state PL spectra were presented in Figure 2d, revealing a sharp emission peak at 621 nm. These red-emitting QDs exhibited a near-unity PL QY of 97% (Figure S3), excellent photostability under continuous excitation (Figure S4), and monoexponential PL decay dynamics (Figure 2e), confirming well-controlled decay dynamics of the band-edge excitons and the suppression of nonradiative decay pathways.

In terms of optical performance, the emission peak of the prepared fluorescent temperature sensor exhibited an approximate 1 nm red shift, along with broadening of the PL spectrum, compared to that of the original QD solution (Figure S5). These phenomena were attributed to self-absorption effects arising from the formation of a dense QD film on the fiber surface. Notably, the subsequent deposition of the Al_2O_3 encapsulation layer did not induce any significant shift in the emission peak, indicating that the protective coating process did not cause substantial damage to the QDs (Figure S5). The PL emission peak position remained remarkably stable under varying integration times (Figures 2f and Supporting Information Figure S6) and excitation intensities (Figure S7), whereas the fluorescence intensity showed a linear dependence. Furthermore, when the excitation wavelength was tuned from 300 to 500 nm, the peak wavelengths of QDs remained unchanged (Figure S8). These behaviors confirmed that the emission wavelength was an intrinsic property, independent of the measurement conditions, thereby validating it as a robust metric for thermometry. Utilizing a fast-acquisition spectrometer, the sensor generated a detectable fluorescence signal with an integration time of <10 μs (Figure S6). This performance, attributed to the outstanding optical properties of the QD probes, confirms excellent temporal resolution and the suitability of sensor for real-time biological temperature monitoring.

The fluorescence microscope images revealed that the QDs were uniformly coated on the tip of tapered fiber with bright red-emission (Figure 2g). Energy-dispersive X-ray spectroscopy (EDS) elemental mapping analysis indicated that the fabricated fiber-optic temperature probe was primarily composed of Cd, Zn, Se, S, Si, O, and Al (Figure 2h). The total thickness of the sensing film was $\sim$ 65 nm, consisting of an approximately 35 nm-thick QD layer and a 30 nm-thick Al_2O_3 protective layer covering it (Figure 2i). The entire structure exhibited excellent uniformity and density, confirming the successful fabrication of the dual-functional architecture.

Stability Evaluation

In fluorescent temperature sensors, the optical stability of the sensing materials is critical for detection accuracy and long-term applicability. However, QDs are prone to degradation during prolonged use, typically manifested as a blue shift in the PL peak and a gradual decay of fluorescence intensity under illumination. This degradation process is primarily induced by surrounding chemical environmental factors, which is mediated through mechanisms including the etching of the inorganic layers and oxidation or dissociation of surface ligands.[44] To

https://doi.org/10.1021/acsnano.6c06731
ACS Nano XXXX, XXX, XXX−XXX

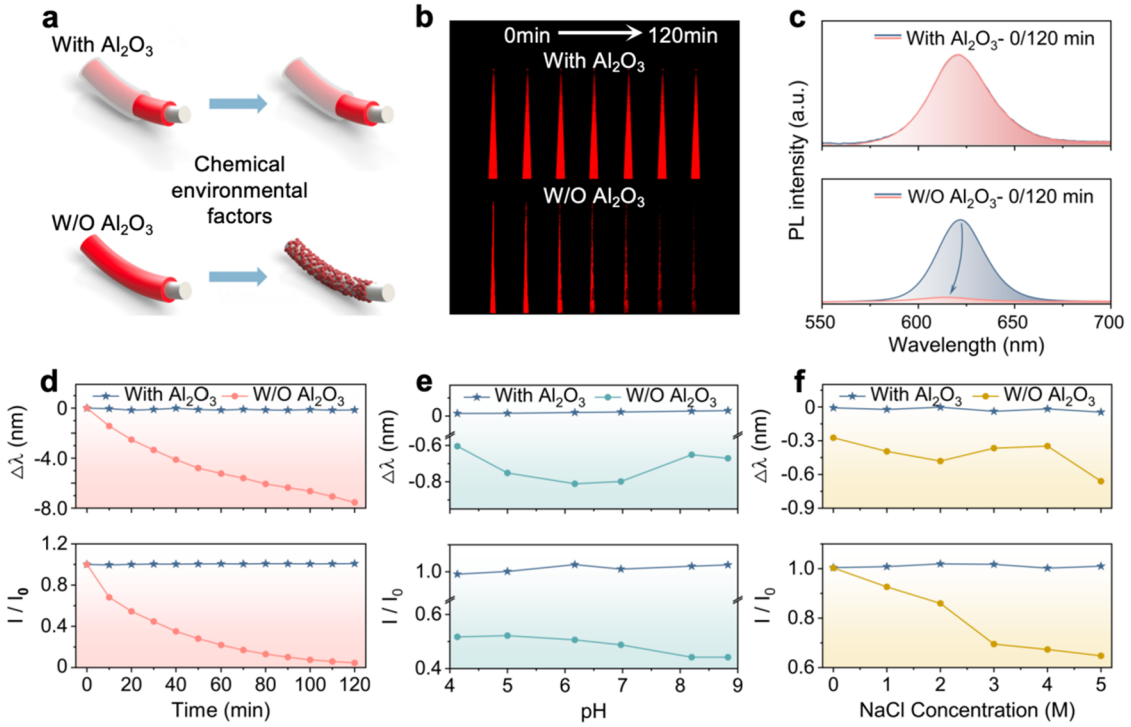

Figure 3. Stability evaluation of QDs-functionalized fiber-optic sensor. (a) Schematic of the etching process for sensors with and without Al_2O_3 protection. (b) Evolution of fluorescence microscopy images and (c) PL spectra of sensors with and without Al_2O_3 coating under continuous UV excitation for 120 min. (d) Variations in PL intensity and emission peak position during 120 min of continuous UV excitation; (e) under varying pH conditions; (f) in NaCl solutions of different concentrations.

address this issue, encapsulating QDs within a dense Al_2O_3 inorganic oxide layer via ALD has proven to be an effective strategy (Figure 3a).

We first investigated the photostability under continuous UV illumination. Fluorescence microscopy images provided a direct visual comparison. As shown in Figure 3b, over time, the fluorescence from the uncoated tip progressively weakened and concurrently lost its spatial uniformity, whereas the Al_2O_3-coated tip demonstrated a bright and homogeneous emission. The scanning electron microscopy (SEM) images revealed that the uncoated sensor surface exhibited severe degradation, characterized by the extensive detachment of QDs and disruption of the surface morphology (Figure S9). This observation was quantitatively confirmed by tracking the evolution of the PL spectra (Figure 3c) and the normalized peak intensity and position over time (Figure 3d). The uncoated sensor suffered a rapid and pronounced decay in fluorescence intensity (>90% loss within 2 h), accompanied by an approximate 8 nm blue shift of the emission peak. This behavior was primarily attributed to photoinduced oxidation and the exacerbation of surface defects, which significantly enhanced nonradiative recombination pathways. In contrast, the Al_2O_3-coated sensor exhibited negligible PL intensity decay and peak wavelength shift under the same conditions, indicating that the Al_2O_3 coating effectively suppressed photodegradation. Throughout the thirty-day continuous spectroscopic testing, both the PL intensity and emission wavelength remained stable with no significant changes observed (Figure S10).

Next, we evaluated the chemical stability of FOQDS against pH variations. As shown in Figure 3e, the uncoated sensor displayed a strong sensitivity to environmental pH, exhibited a reduction of more than 50% in fluorescence intensity in strongly acidic or basic solutions, and was accompanied by a dramatic blue shift of the peak position. This was attributed to surface protonation/deprotonation and etching of the QDs. In contrast, the Al_2O_3-coated sensor demonstrated remarkable insensitivity to pH, with both the PL intensity and peak position remaining virtually constant, thus ensuring reliable performance in diverse biological microenvironments. The stability against ionic influence was tested in NaCl solutions of varying concentrations (Figure 3f). Similarly, the uncoated sensor experienced significant fluorescence quenching and spectral shifts at high salt concentrations, whereas the Al_2O_3 layer effectively shielded the QDs, as made evident by the stable fluorescence signal of the coated sensor across the entire concentration range. These results indicated that the dense and chemically stable Al_2O_3 coating provides a robust barrier for QDs, significantly mitigating the degradation of their optical properties. This advantage ensured the stable operation of the FOQDS under prolonged illumination, extreme pH conditions, and high-salinity environments, providing strong assurance for its application in fields requiring long-term stability such as biosensing, clinical diagnostics, and environmental monitoring.

Performance of FOQDS

We systematically evaluated the temperature response characteristics of the prepared temperature sensor. The PL spectra of the sensor were acquired across a physiologically critical range from 25 to 50 °C. As shown in Figure 4a, the emission spectra exhibited a continuous and monotonic redshift with increasing temperature, which was attributed to the temperature-induced shrinkage of the QD bandgap and the enhanced exciton-LO phonon scattering, while the spectral shape remains unchanged. The PL peak wavelength exhibited

https://doi.org/10.1021/acsnano.6c06731
ACS Nano XXXX, XXX, XXX−XXX

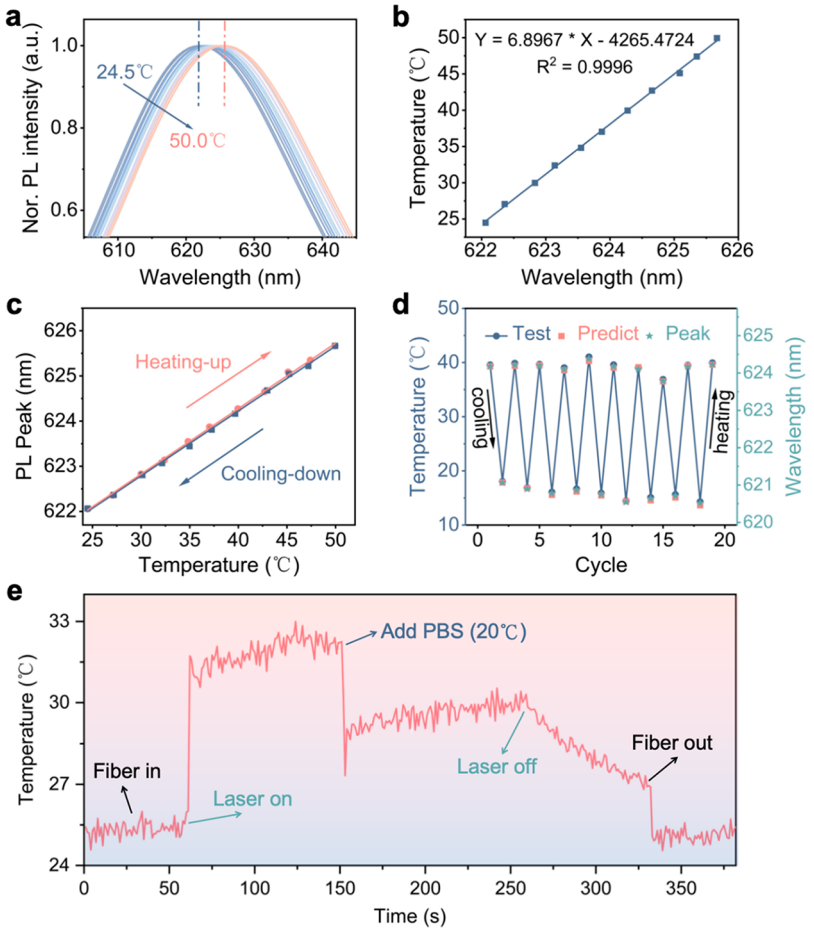

Figure 4. Optical temperature sensing properties. (a) PL spectra of FOQDS to a temperature ranging from 24.5 to 50.0 °C. (b) Calibration curve of the temperature sensor for sensing in PBS. (c) Repeatability of temperature measurements during heating and cooling cycles. (d) Comparison between the FOQDS and a commercial thermocouple. (e) Real-time temperature monitoring during laser heating, PBS cooling, and system recovery.

an excellent linear dependence on temperature (R^2 = 0.9996), with a sensitivity of 145 pm/°C (Figure 4b). This well-defined linear calibration was paramount for straightforward and accurate temperature extraction. A monotonic blue shift of the emission peak was observed during cooling (Figure S11). The robust reversibility and stability of the temperature sensor were confirmed by the complete overlap of the PL spectra at the start and end of a thermal cycle (Figure S11), as well as by the virtually identical heating and cooling calibration curves (Figure 4c).

To validate the measurement accuracy against established standards, we compared the temperature readings from our FOQDS with those from a calibrated commercial thermocouple during repeated switching between different temperature set points. The results demonstrated consistency between the two methods across nine consecutive alternating temperature cycles, as presented in Figure 4d. This independent verification confirmed that our sensor provided accurate and reliable temperature values, not merely relative changes. Furthermore, FOQDS probes fabricated from different batches yielded highly overlapping wavelength−temperature curves (Figure S12), confirming negligible interfiber variation and excellent batch-to-batch reproducibility.

Next, we demonstrated the capability of our sensor for real-time thermal monitoring in a simulation temperature-changing process. The sensor probe was inserted into the culture medium to monitor the localized microenvironment. For controlled thermal perturbation, a focused high-power 1550 nm infrared laser was delivered via a separate optical fiber positioned near the sensor probe to enable localized heating. As illustrated in Figure 4e, upon activating the infrared laser for localized heating, a sharp transition step with high amplitude and steep edges was observed, indicating the rapid response of the sensor to ambient temperature variations. Subsequently, cold PBS buffer solution (0.5 mL, ∼ 20 °C) was added into the culture medium, causing a sharp and transient temperature drop, which was instantly and accurately captured by the sensor in real time. The system then re-equilibrated to a steady-state temperature under continuous laser heating. When the laser was turned off, the sensor tracked the slow cooling of the microenvironment until the probe was removed from the medium, at which point the signal returned to the baseline room temperature. This experiment demonstrated high temporal resolution and great sensitivity of the optical fiber sensor for monitoring thermal dynamics in complex media environments.

FOQDS Measured Real-Time Cell-Spheroid Temperature toward Single-Cellular Resolution

Three-dimensional (3D) glioblastoma spheroids constitute physiologically relevant in vitro models that more faithfully recapitulate the architectural, metabolic, and signaling

https://doi.org/10.1021/acsnano.6c06731
ACS Nano XXXX, XXX, XXX−XXX

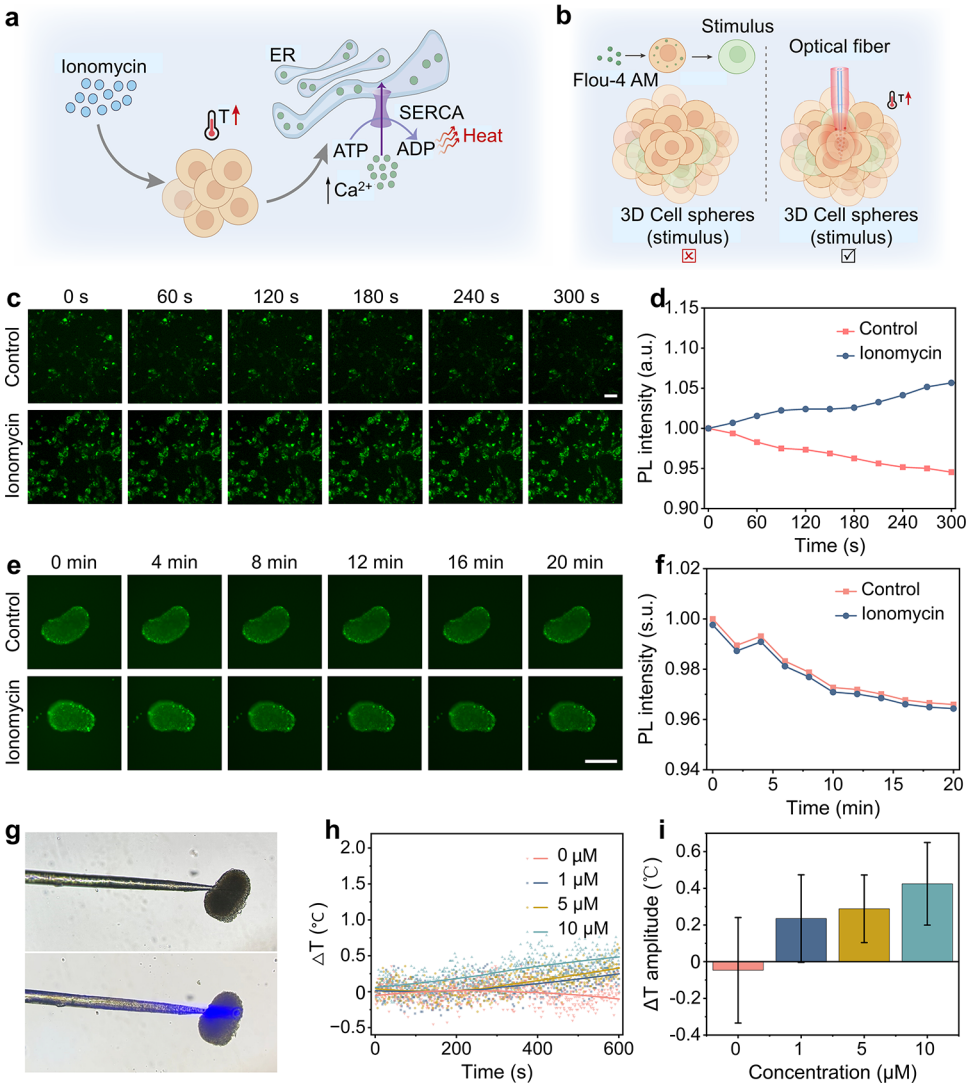

Figure 5. In situ temperature monitoring of GSC-PNT under ionomycin stimulation. (a) Schematic of SERCA-mediated Ca^{2+} transport into the endoplasmic reticulum following ionomycin treatment, accompanied by ATP hydrolysis−driven heat generation. (b) Comparison of conventional fluorescence probe−based temperature detection and FOQDS-based sensing in 3D spheroids. (c) Fluo-4 AM fluorescence images of glioblastoma stem cells stimulated with ionomycin for 300 s, with Ca^{2+}-free PBS as the control. (d) Time-resolved quantification of intracellular Ca^{2+} fluorescence intensity corresponding to panel (c). (e) Fluo-4 AM fluorescence images of glioblastoma stem cell spheroids after 20 min of ionomycin stimulation, with Ca^{2+}-free PBS as control. (f) Quantitative analysis of fluorescence intensity corresponding to panel (e). (g) Microscopic images of spheroids before and after tapered fiber insertion for QD excitation. (h) Real-time temperature profiles of spheroids monitored by the FOQDS upon ionomycin stimulation (1, 5, and 10 μM) over 600 s. (i) Quantitative analysis of ΔT amplitudes, revealing concentration-dependent thermal responses. (scale bar, 100 μm, n = 3).

characteristics of native tumor microenvironments than conventional monolayer cultures.[11] These spheroids exhibit elevated metabolic activity and heightened sensitivity to calcium signaling, both of which are central features of the tumor physiology. Previous studies have shown that ionomycin, a well-established calcium ionophore, induces rapid intracellular Ca^{2+} influx and activates sarco/endoplasmic reticulum Ca^{2+}-ATPase (SERCA), thereby driving Ca^{2+} reuptake into the endoplasmic reticulum (ER).[45] This reuptake process is ATP-dependent and intrinsically thermogenic, releasing heat as a metabolic byproduct and leading to localized extracellular temperature elevations (Figure 5a).[46,47] Such physiologically induced, spatially confined thermal signals in metabolically active 3D tumor spheroids provide a stringent and biologically relevant platform for benchmarking in situ temperature sensing strategies.

To evaluate the performance of FOQDS in complex multicellular environments, we monitored ionomycin-induced temperature fluctuations in glioblastoma stem cell spheroids (GSC-PNT) in real time. As a benchmark, we directly compared this fiber-based approach with conventional fluorescent temperature probing for spheroid temperature readout (Figure 5b). At the single-cell level, Fluo-4 acetoxymethyl ester (Fluo-4 AM) calcium imaging revealed increases in intracellular Ca^{2+} within 150 s following ionomycin stimulation (Figure 5c), and quantitative analysis showed rise in fluorescence intensity (Figure 5d). This single-cellular-scale resolution fluorescence measurement successfully captured the expected calcium dynamics that underlie thermogenic activity. However, when extended to intact 3D spheroids, bulk fluorescence imaging failed to resolve dynamic intracellular responses even after 20 min of ionomycin

https://doi.org/10.1021/acsnano.6c06731
ACS Nano XXXX, XXX, XXX−XXX

treatment (Figure 5e), with corresponding quantitative analysis showing negligible signal changes (Figure 5f). These results highlight a fundamental limitation of conventional fluorescence-based probing in 3D systems, where light scattering, limited penetration depth and averaging over heterogeneous cellular populations obscure subtle but physiologically meaningful temperature fluctuations.

In contrast, the FOQDS can be directly inserted into the 3D spheroid, enabling localized excitation and temperature readout at defined intratissue positions without disrupting the overall architecture (Figure 5g). Biosafety assessments confirmed that the fiber sensor exhibited good long-term biocompatibility (Figures S13 and S14). SEM images further showed no obvious structural disruption or mechanical damage in spheroids following FOQDS insertion (Figure S15). Supporting experiments confirmed that the excitation light induces negligible local heating and no measurable phototoxicity under the relevant exposure conditions (Figures S16 and S17). Upon ionomycin stimulation, the fiber-based probe robustly captured real-time extracellular temperature elevations within the spheroid (Figure 5h). Quantitative analysis further revealed a clear dependence of the temperature increase (ΔT) on ionomycin concentration (Figure 5i). Notably, despite operating in a densely packed 3D cellular environment where bulk fluorescence measurements fail, the fiber sensor reliably resolved subtle thermogenic signals, effectively achieving functional sensitivity comparable to state-of-the-art fluorescent temperature probes.

We performed finite-element simulations of the cell-spheroid thermometry experiment. First, we modeled the cell spheroid as a heat source that gradually increases over time; the temperature of the inserted optical fiber rose accordingly, reaching a temperature increase of approximately 0.5 K after 600 s (Figure S18). We then simulated different insertion depths and found that the measurement results remained essentially unchanged (Figure S19). These simulations indicate that our method holds promise for achieving single-cell resolution measurements in the future. When the simulated heat source was reduced to the size of a single cell, the fiber could not be inserted into the cell, but it could be heated by the surrounding water (Figure S20). Moreover, a higher-precision taper-drawing method could be employed in the future to fabricate even smaller microfibers, which would exert an even smaller perturbation on the temperature field around the cell (Figure S21). The temperature increase in the fiber can ultimately be transduced into a shift of the fluorescence peak of the quantum dots at the fiber tip, which has the potential to be monitored experimentally. We further note that insertion of the tapered fiber probe may introduce local perturbations, such as transient membrane disruption or altered heat transport. In practice, the probe tip is less than 20 μm in diameter and is positioned gently under microscopic guidance. Although the glass fiber can act as a thermal sink, the thermal mass of the tapered tip is very small, and given the spheroid size and the transient thermal events studied here, the resulting thermal perturbation is expected to be limited and unlikely to significantly alter the recorded temperature dynamics. During our measurements, we did not observe obvious signs of acute membrane damage or drastic thermal alteration. Therefore, these minor perturbations do not compromise the dynamic thermal measurements reported in this work.

As suggested by the above results, FOQDS enables precise in situ thermal mapping within complex 3D tumor spheroids. By circumventing the depth-related and signal-averaging limitations inherent to conventional fluorescent approaches, this platform establishes a powerful and complementary methodology for probing the coupling among cellular energy metabolism, calcium signaling, and pharmacological perturbation in physiologically relevant tumor-like architectures.

CONCLUSIONS

In summary, we report a highly sensitive and stable fiber-optic QDs sensor (FOQDS) for real-time, quantitative thermal monitoring toward the single-cellular scale. By integrating with a conformal Al_2O_3 encapsulation layer, FOQDS achieves high spatiotemporal resolutions, good long-term optical and chemical stability, and linear temperature response within physiologically relevant ranges. The miniaturized probe enables minimally invasive insertion into 3D tumor spheroids, allowing quantitative and real-time monitoring of subtle, localized extracellular temperature fluctuations induced by pharmacological stimuli over extended periods, which is unattainable with conventional fluorescence imaging. This work not only provides an innovative tool for fundamental biology research but also paves the way for advanced diagnostics and personalized medicine by enabling direct observation of metabolic thermal signatures at the cellular level. Moreover, the FOQDS platform is inherently extensible, not only to other QDs systems such as near-infrared-emitting or cadmium-free alternatives for deeper tissue penetration or multiplexed sensing but also toward spatial thermal mapping via multipoint or scanning configurations, thereby enabling more complex biological models and advanced diagnostic applications.

EXPERIMENTAL SECTION

Chemicals

Cadmium oxide (CdO, 99.99%), cadmium acetate ($Cd(Ac)_2{\cdot}2H_2O$, 99.9%), zinc acetate ($Zn(Ac)_2$, 99.99%), selenium (99.99%), sulfur (99.98%), 1-octadecene (ODE, 90%), oleic acid (90%), myristic acid (99%), and capric acid (98%) were purchased from Sigma-Aldrich. Sodium chloride (NaCl) were obtained from General-Regent. Chloroform, DMEM/F12 medium, Nonessential Amino Acids, Sodium Pyruvate, GlutaMAX, Penicillin/Streptomycin/Amphotericin, B-27 supplement, bFGF, EGF and Heparin were purchased from Gibco. Fluo-4 AM (calcium ion fluorescence probe, 2 mM) were acquired from Beyotime Biotechnology. CCK-8 was purchased from Meilunbio. Ionomycin was purchased from Sigma-Aldrich. Trimethylaluminum (TMA) was purchased from APK (Shanghai) Gas Co., Ltd.

Materials Characterization

Steady-state PL spectra were measured via an Edinburgh FS5 spectrofluorometer. Transient PL spectra were obtained via the time-correlated single-photon counting (TCSPC) method with a 450 nm picosecond laser diode. The absolute PL QYs were obtained via integrating sphere coupling with an Ocean Optics QE Pro spectrometer. Fluorescence spectra at different integration times were acquired by using an Ocean Optics QE Pro spectrometer and an Ocean Optics FX spectrometer. TEM images were collected on a Thermo Scientific Talos L120C TEM instrument operated at 80 kV. The HRTEM images, the HAADF-STEM images, and the corresponding EDS elemental mapping were obtained by Thermo Scientific Talos F200X STEM operated at 200 kV. SEM was carried out on a Thermo Scientific Scios2 Hivac. The crystallinity of samples was examined by XRD using a Bruker D2 Phaser diffractometer. Fluorescence micrographs were acquired by using a Nikon ECLIPSE Ti2 inverted microscope.

https://doi.org/10.1021/acsnano.6c06731
ACS Nano XXXX, XXX, XXX−XXX

Preparation of QDs

Preparation of CdSe Core QDs. Cadmium oxide (0.01 mmol), myristic acid (0.028 mmol), and 1-octadecene (4 mL) were combined in a reaction vessel. Under continuous argon flow with stirring, the solution was heated to 250 °C. A preprepared Se-SUS (1 mL, 0.06 mol/L) was swiftly injected into the reaction. The system temperature was then maintained at 240 °C. After 5 min of reaction, the Se-SUS (0.1 mol/L) was added dropwise at a constant rate via a syringe pump to control the growth of QDs until the desired size was achieved.

Preparation of CdSe/CdS Core/Shell QDs. Cadmium acetate (0.7 mmol), capric acid (0.7 mmol), oleic acid (2.1 mmol), and 1-octadecene (4 mL) were mixed and heated to 160 °C under argon protection with stirring. Purified CdSe core QD solution was then introduced, and the reaction temperature was promptly raised to 260 °C. S-ODE (0.1 mol/L) was added dropwise at a set rate (2 mL/h) using a syringe pump until the core/shell structure reached the intended thickness.

Preparation of CdSe/CdS/ZnS Core/Shell/Shell QDs. Zinc acetate (0.5 mmol), capric acid (0.4 mmol), oleic acid (1.1 mmol), and 1-octadecene (4 mL) were placed in a reaction flask and degassed by argon bubbling for 7 min, followed by heating to 150 °C. Purified CdSe/CdS core/shell QDs were injected, and the temperature was then programmatically increased to 300 °C. At this temperature, S-ODE (0.2 mol/L) was added dropwise at a fixed rate. Once the product reached the target size, the heat source was immediately removed to terminate the reaction.

Preparation of FOQDS

Fabrication of Tapered Optical Fiber. The tapered optical fiber was fabricated from a standard step-index multimode fiber with a cladding diameter of 125 μm and a core diameter of 105 μm. The standard optical fiber was securely mounted on two displacement stages. Positioned between these stages was a heating flame, which rapidly elevated the temperature of the exposed optical fiber with the coating removed. As the fiber was heated and softened, the displacement stages simultaneously stretched the fiber outward at a controlled rate. Within the heating zone, the optical fiber was drawn into a tapered structure with a uniformly decreasing diameter. Ultimately, by precisely controlling the displacement stages to continue stretching for a predetermined distance, the fiber fractured at the thinnest point within the conical region, resulting in two independent optical fiber tapers. By implementing a programmed stretching protocol, this fabrication process could be automated to produce optical fiber tapers with specified taper angles and tip diameters.

Fabrication of QDs Coating. The tapered optical fiber was immersed in a solution of CdSe/CdS/ZnS core/shell/shell QDs (10 mg/mL in chloroform) for several seconds and then withdrawn to allow the solvent to evaporate. This dipping process was repeated five times to ensure that sufficient QDs adhered to the fiber surface.

Fabrication of Protective Layer. An Al_2O_3 protective layer was deposited on the QDs-coated tapered optical fiber by atomic layer deposition (MNT-S system). The deposition was performed at 170 °C for 300 cycles.

FOQDS Stability Characterization

The stability of continuous temperature monitoring was measured. The PL spectra of the proposed optical fiber sensing setup in PBS (25 °C, pH= 7.4) solution were recorded every 1 min for a continuous 120 min monitoring. The pH stability of the FOQDS was tested by placing the prepared FOQDS in a microplate well and immersing it in 5 mL of pH standard solution (pH= 4.1, 5, 6.2, 7, 8.2, and 8.8). After the signal stabilized, the PL spectrum was collected and the shift of the spectral peak with pH was determined. The ion stability of the FOQDS was tested by placing the prepared FOQDS in a microplate well and immersing it in 5 mL of NaCl solution at varying concentrations (0, 1, 2, 3, 4, 5 M, pH 7.4). After the signal stabilized, the PL spectrum was collected and the shift of the spectral peak with ion concentration was determined.

Temperature Dependence Test of FOQDS

FOQDS Calibration Curve. The FOQDS was characterized in PBS (1×, pH= 7.4). A hot plate was used to adjust the buffer temperature, which was monitored by a portable thermometer to precisely control temperature variations. The sensor was immersed in PBS solutions with temperature ranging from approximately 25 to 50 °C. PL spectra were acquired, and the spectra peak shift with temperature was calculated.

Corresponding Real-Time Measurement. The FOQDS was placed in PBS (1×, pH= 7.4). A fiber delivering a 1550 nm laser was positioned near the tip as a heat source to achieve localized heating of the solution. The thermal environment was modulated by applying localized 1550 nm laser heating, introducing cold PBS, and then turning off the heating laser. The PL spectrum was measured and the PL peak position was calculated for each measurement.

Determination of Fluorescence Intensity at Different Integration Times. The FOQDS was placed in PBS (1×, pH= 7.4), and after the signal was stabilized, the PL spectra were collected at different integration times (8−500 ms and 10 μs to 10 ms).

Cell Experiment

Cell Culture. Mouse neural stem cells with Trp53, Pten, and Nf1 deletions were transplanted into the mouse brain to induce glioma, from which glioblastoma stem cells (GSCs) were isolated. GSC-PNT cells display stem-like properties and require specific conditions to maintain stemness and support spontaneous sphere formation. Cells were cultured in basal GSC medium consisting of DMEM/F12 (3:1) (Gibco) supplemented with 1× nonessential amino acids, 1 mM sodium pyruvate, 2 mM GlutaMAX, and 1× penicillin/streptomycin/amphotericin. A 50× supplement cocktail containing B-27, basic fibroblast growth factor (bFGF, 1 μg/μL), epidermal growth factor (EGF, 1 μg/μL), and heparin (250 ng/μL) was freshly prepared and added to the basal medium at a 1:50 dilution to generate complete GSC medium immediately prior to use. Cells were seeded onto low-attachment plates, and spheroid formation was typically observed within 7−10 days, depending on proliferation rate. Spheres with diameters of 50−200 μm were considered optimal for activity and uniformity and were monitored under a microscope.

Biocompatibility of the FOQDS Sensor. GSC-PNT cells were employed for in vitro cytotoxicity evaluation via the Cell Counting Kit-8 (CCK-8) assay. Cells were seeded and allowed to stabilize for 4 h before adding sterilized fiber or FOQDS segments (~1 cm in length) to the designated wells. After coincubation for 24 h, the cells were washed with PBS, and CCK-8 reagent (Meilunbio) was added to each well at a reagent-to-medium ratio of 1:10. Plates were incubated for 2 h at 37 °C in the dark, and absorbance was measured at 450 nm using a microplate reader. Cell viability was calculated as the percentage relative to the Control group after subtraction of the background (medium + CCK-8 without cells).

Long-Term Biocompatibility of the FOQDS Sensor. Sterilized FOQDS segments (~1 cm in length) were immersed in complete culture medium and incubated at 37 °C for 1, 3, 5, or 7 days to obtain extraction media. GSC-PNT cells were cultured with the extraction media, and cell viability was evaluated using a Cell Counting Kit-8 (CCK-8) assay. Cells were seeded and allowed to stabilize for 4 h before replacing the original medium with the corresponding extraction media. After incubation for 24 h, the cells were washed with PBS, and CCK-8 reagent (Meilunbio) was added to each well at a reagent-to-medium ratio of 1:10. Plates were incubated for 2 h at 37 °C in the dark, and absorbance was measured at 450 nm using a microplate reader. Cell viability was calculated as the percentage relative to the Control group after subtraction of the background (medium + CCK-8 without cells).

SEM Characterization of Spheroid Morphology after FOQDS Insertion. An FOQDS temperature sensor was gently inserted into the center of GSC-PNT spheroids using a micromanipulator under a stereomicroscope with untreated spheroids used as controls. The spheroids were then washed three times with PBS, fixed in 2.5% glutaraldehyde for 2 h, dehydrated through a graded ethanol series (30%, 50%, 70%, 80%, 90%, and 100%), and transferred

https://doi.org/10.1021/acsnano.6c06731
ACS Nano XXXX, XXX, XXX−XXX

to silicon wafers for drying. The samples were subsequently sputter-coated with gold and examined by SEM.

Monitoring of Intracellular [Ca^{2+}] Variations in Single GSC−PNT Cells under Chemical Stimulation. To investigate intracellular [Ca^{2+}] dynamics in response to chemical stimulation, single GSC−PNT cells were incubated with 2 μM Fluo-4 AM in Ca^{2+}-free culture medium at 37 °C for 1 h. After incubation, the cells were washed three times with PBS to remove excess dye. Subsequently, cells were treated with ionomycin (10 μM) to induce Ca^{2+} influx, and fluorescence imaging was immediately performed. As a control, 1 mL of Ca^{2+}-free culture medium without ionomycin was added to Fluo-4 AM−loaded cells. The temporal variations of intracellular [Ca^{2+}] were monitored by recording the fluorescence intensity of Fluo-4 within 300 s after ionomycin stimulation for 60 s.

Monitoring of Intracellular [Ca^{2+}] Variations in GSC−PNT Spheroids under Chemical Stimulation. To investigate intracellular [Ca^{2+}] dynamics in response to chemical stimulation, GSC−PNT spheroids were incubated with 2 μM Fluo-4 AM in Ca^{2+}-free culture medium at 37 °C for 1 h. After incubation, the spheroids were gently washed three times with PBS to remove excess dye. Subsequently, spheroids were treated with ionomycin (10 μM) to induce Ca^{2+} influx, followed by fluorescence imaging. As a control, 1 mL of Ca^{2+}-free culture medium without ionomycin was added to Fluo-4 AM−loaded spheroids. The temporal variations of intracellular [Ca^{2+}] within spheroids were recorded by monitoring the fluorescence intensity of Fluo-4 over 20 min.

Temperature Measurement in GSC−PNT Spheroids under Ionomycin Stimulation with FOQDS. To evaluate temperature variations within GSC−PNT spheroids under ionomycin stimulation, an FOQDS temperature sensor was gently inserted into the center of individual spheroids using a micromanipulator under a stereomicroscope. The sensor was connected to the optical detection system for optical signal acquisition, which was subsequently processed to calculate the temperature changes. After signal stabilization, spheroids were treated with ionomycin at 1, 5, and 10 μM, respectively, to induce intracellular Ca^{2+} influx in the spheroids. Optical signals were continuously recorded, and the temperature evolution within the spheroids was derived from the acquired data. Control measurements were performed by adding an equal volume of Ca^{2+}-free culture medium without ionomycin.

■ ASSOCIATED CONTENT

Supporting Information

The Supporting Information is available free of charge at https://pubs.acs.org/doi/10.1021/acsnano.6c06731.

Simulated laser and fluorescence energy distribution in tapered fiber; optical and structural characterization of CdSe and CdSe/CdS QDs; PL QY of CdSe/CdS/ZnS QDs; PL spectra of QD solutions and sensors with/without Al_2O_3 encapsulation; integration time dependence; effect of excitation intensity and excitation wavelength on fluorescence; SEM morphology before/after continuous excitation; long-term stability over 30 days; temperature response, batch-to-batch reproducibility and reversibility of FOQDS; biocompatibility evaluation; mechanical impact assessment; photothermal and phototoxicity assessment (PDF)

■ AUTHOR INFORMATION

Corresponding Authors

Xuanyong Liu − *School of Chemistry and Materials Science, Hangzhou Institute for Advanced Study, University of Chinese Academy of Sciences, Hangzhou 310024, China; State Key Laboratory of High Performance Ceramics, Shanghai Institute of Ceramics, Chinese Academy of Sciences, Shanghai 200050, China; University of Chinese Academy of Sciences, Beijing 100049, China;* orcid.org/0000-0001-9440-8143; Email: xyliu@mail.sic.ac.cn

Jizhai Cui − *International Institute for Intelligent Nanorobots and Nanosystems & State Key Laboratory of Surface Physics, College of Intelligent Robotics and Advanced Manufacturing, Fudan University, Shanghai 200438, China; Zhejiang Key Laboratory of Extreme Environment Functional Materials, Yiwu Research Institute of Fudan University, Yiwu 322000, China;* orcid.org/0000-0003-1317-0570; Email: jzcui@fudan.edu.cn

Kewang Nan − *State Key Laboratory of Advanced Drug Delivery and Release Systems, School of Pharmacy, Zhejiang University, Hangzhou 310058, China; Hangzhou Institute of Innovative Medicine, School of Pharmacy, Zhejiang University, Hangzhou 310058, China*; Email: knan@zju.edu.cn

Xiaoqi Hou − *School of Chemistry and Materials Science, Hangzhou Institute for Advanced Study, University of Chinese Academy of Sciences, Hangzhou 310024, China; University of Chinese Academy of Sciences, Beijing 100049, China;* orcid.org/0000-0002-5449-2034; Email: houxiaoqi@ucas.ac.cn

Authors

Dongliang Hu − *School of Chemistry and Materials Science, Hangzhou Institute for Advanced Study, University of Chinese Academy of Sciences, Hangzhou 310024, China; State Key Laboratory of High Performance Ceramics, Shanghai Institute of Ceramics, Chinese Academy of Sciences, Shanghai 200050, China; University of Chinese Academy of Sciences, Beijing 100049, China*

Jialu Zhang − *State Key Laboratory of Advanced Drug Delivery and Release Systems, School of Pharmacy, Zhejiang University, Hangzhou 310058, China; Hangzhou Institute of Innovative Medicine, School of Pharmacy, Zhejiang University, Hangzhou 310058, China*

Yang Zong − *International Institute for Intelligent Nanorobots and Nanosystems & State Key Laboratory of Surface Physics, College of Intelligent Robotics and Advanced Manufacturing, Fudan University, Shanghai 200438, China; Zhejiang Key Laboratory of Extreme Environment Functional Materials, Yiwu Research Institute of Fudan University, Yiwu 322000, China*

Minjie Xi − *International Institute for Intelligent Nanorobots and Nanosystems & State Key Laboratory of Surface Physics, College of Intelligent Robotics and Advanced Manufacturing, Fudan University, Shanghai 200438, China; Zhejiang Key Laboratory of Extreme Environment Functional Materials, Yiwu Research Institute of Fudan University, Yiwu 322000, China*

Luxi Hu − *School of Chemistry and Materials Science, Hangzhou Institute for Advanced Study, University of Chinese Academy of Sciences, Hangzhou 310024, China; State Key Laboratory of High Performance Ceramics, Shanghai Institute of Ceramics, Chinese Academy of Sciences, Shanghai 200050, China; University of Chinese Academy of Sciences, Beijing 100049, China*

Kaijie Zhu − *School of Chemistry and Materials Science, Hangzhou Institute for Advanced Study, University of Chinese Academy of Sciences, Hangzhou 310024, China; University of Chinese Academy of Sciences, Beijing 100049, China*

https://doi.org/10.1021/acsnano.6c06731
ACS Nano XXXX, XXX, XXX−XXX

Zhipeng Zhu − *Institute of Biochemistry, College of Life Sciences, Zhejiang University, Hangzhou 310058, China*
Liang Xu − *Institute of Biochemistry, College of Life Sciences, Zhejiang University, Hangzhou 310058, China*
Yongfeng Mei − *International Institute for Intelligent Nanorobots and Nanosystems & State Key Laboratory of Surface Physics, College of Intelligent Robotics and Advanced Manufacturing, Fudan University, Shanghai 200438, China; Zhejiang Key Laboratory of Extreme Environment Functional Materials, Yiwu Research Institute of Fudan University, Yiwu 322000, China;* orcid.org/0000-0002-3314-6108

Complete contact information is available at: https://pubs.acs.org/10.1021/acsnano.6c06731

Author Contributions

◆D.L.H., J.L.Z., and Y.Z. contributed equally to this work. X.Y.L., J.Z.C., K.W.N., and X.Q.H. conceived and designed the project. D.L.H. and Y.Z. prepared and characterized the samples. D.L.H., Y.Z., and J.L.Z. performed the cellular experiments. M.J.X. was responsible for the preliminary simulation. L.X.H. performed the SEM characterizations. D.L.H and K.J.Z. was responsible for the preliminary platform setup. J.L.Z. conducted the cellular experiments, and L.X. and Z.P.Z. provided the cells. Y.F.M. participated in discussing the results. X.Y.L., J.Z.C., K.W.N., and X.Q.H. coordinated and supervised the project. The manuscript was written with discussions and contributions from all authors.

Notes

The authors declare no competing financial interest.

■ ACKNOWLEDGMENTS

This work was supported by the National Key Technologies R&D Program of China (2022YFA1207000), Basic Public Research Program of Zhejiang Province (LY23B010001), the Key Research and Development Program of Zhejiang Province (2024C03080), the National Natural Science Foundation of China (32270746 and 62504200), and the Research Funds of Hangzhou Institute for Advanced Study, UCAS (2023HIAS-Y020).

■ REFERENCES

(1) Okabe, K.; Inada, N.; Gota, C.; Harada, Y.; Funatsu, T.; Uchiyama, S. Intracellular Temperature Mapping with a Fluorescent Polymeric Thermometer and Fluorescence Lifetime Imaging Microscopy. *Nat. Commun.* **2012**, *3* (1), No. 705.
(2) Zhang, M.; Zhang, B.; Liu, C.; Preußner, M.; Ayachit, M.; Li, W.; Huang, Y.; Liu, D.; He, Q.; Emmerichs, A.-K.; Meinke, S.; Chen, S.; Wang, L.; Zheng, L.; Li, Q.; Huang, Q.; Haltenhof, T.; Gao, R.; Qin, X.; Cheng, A.; Wei, T.; Yu, L.; Schubert, M.; Gao, X.; Li, M.; Heyd, F. Stabilizing a Mammalian RNA Thermometer Confers Neuroprotection in Subarachnoid Hemorrhage. *Nat. Commun.* **2025**, *16* (1), No. 8319.
(3) Li, Y.; Ivica, N. A.; Dong, T.; Papageorgiou, D. P.; He, Y.; Brown, D. R.; Kleyman, M.; Hu, G.; Chen, W. W.; Sullivan, L. B.; Del Rosario, A.; Hammond, P. T.; Vander Heiden, M. G.; Chen, J. MFSD7C Switches Mitochondrial ATP Synthesis to Thermogenesis in Response to Heme. *Nat. Commun.* **2020**, *11* (1), No. 4837.
(4) Company-Garrido, I.; Carpio, A. Z.; Colomer-Rosell, M.; Ciraulo, B.; Molkenbur, R.; Lanzerstorfer, P.; Pezzano, F.; Agazzi, C.; Hauschild, R.; Jain, S.; Jacques, J. M.; Venturini, V.; Knapp, C.; Xie, Y.; Merrin, J.; Weghuber, J.; Schaaf, M.; Quidant, R.; Kiermaier, E.; Arroyo, J. O.; Ruprecht, V.; Wieser, S. Myosin II Regulates Cellular Thermo-Adaptability and the Efficiency of Immune Responses. *Dev. Cell* **2025**, *61*, 356−371.
(5) Benman, W.; Huang, Z.; Iyengar, P.; Wilde, D.; Mumford, T. R.; Bugaj, L. J. A Temperature-Inducible Protein Module for Control of Mammalian Cell Fate. *Nat. Methods* **2025**, *22* (3), 539−549.
(6) Di, X.; Wang, D.; Su, Q. P.; Liu, Y.; Liao, J.; Maddahfar, M.; Zhou, J.; Jin, D. Spatiotemporally Mapping Temperature Dynamics of Lysosomes and Mitochondria Using Cascade Organelle-Targeting Upconversion Nanoparticles. *Proc. Natl. Acad. Sci. U.S.A.* **2022**, *119* (45), No. e2207402119.
(7) Chuma, S.; Kiyosue, K.; Akiyama, T.; Kinoshita, M.; Shimazaki, Y.; Uchiyama, S.; Sotoma, S.; Okabe, K.; Harada, Y. Implication of Thermal Signaling in Neuronal Differentiation Revealed by Manipulation and Measurement of Intracellular Temperature. *Nat. Commun.* **2024**, *15* (1), No. 3473.
(8) Ding, H.; Liu, K.; Zhao, X.; Su, B.; Jiang, D. Thermoelectric Nanofluidics Probing Thermal Heterogeneity inside Single Cells. *J. Am. Chem. Soc.* **2023**, *145* (41), 22433−22441.
(9) Zhou, H.; Yao, W.; Zhou, X.; Dong, S.; Wang, R.; Guo, Z.; Li, W.; Qin, C.; Xiao, L.; Jia, S.; Wu, Z.; Li, S. Accurate Visualization of Metabolic Aberrations in Cancer Cells by Temperature Mapping with Quantum Coherence Modulation Microscopy. *ACS Nano* **2023**, *17* (9), 8433−8441.
(10) Madhvapathy, S. R.; Bury, M. I.; Wang, L. W.; Ciatti, J. L.; Avila, R.; Huang, Y.; Sharma, A. K.; Rogers, J. A. Miniaturized Implantable Temperature Sensors for the Long-Term Monitoring of Chronic Intestinal Inflammation. *Nat. Biomed. Eng.* **2024**, *8*, 1040−1052, DOI: 10.1038/s41551-024-01183-w.
(11) Rauner, G.; Gupta, P. B.; Kuperwasser, C. From 2D to 3D and beyond: The Evolution and Impact of in Vitro Tumor Models in Cancer Research. *Nat. Methods* **2025**, *22* (9), 1776−1787.
(12) Kiyonaka, S.; Kajimoto, T.; Sakaguchi, R.; Shinmi, D.; Omatsu-Kanbe, M.; Matsuura, H.; Imamura, H.; Yoshizaki, T.; Hamachi, I.; Morii, T.; Mori, Y. Genetically Encoded Fluorescent Thermosensors Visualize Subcellular Thermoregulation in Living Cells. *Nat. Methods* **2013**, *10* (12), 1232−1238.
(13) Liu, L.; Zhang, D.; Bai, P.; Mao, Y.; Li, Q.; Guo, J.; Fang, Y.; Ma, R. Strong Tough Thermogalvanic Hydrogel Thermocell with Extraordinarily High Thermoelectric Performance. *Adv. Mater.* **2023**, *35* (32), No. 2300696.
(14) Zhang, D.; Fang, Y.; Liu, L.; Zhou, Y.; Bai, P.; Li, Q.; Guo, J.; Ma, R. Boosting Thermoelectric Performance of Thermogalvanic Hydrogels by Structure Engineering Induced by Liquid Nitrogen Quenching. *Adv. Energy Mater.* **2024**, *14* (10), No. 2303358.
(15) Yu, X.; Li, S.; Liu, S.; Qiu, J.; Yang, L.; Guo, Y.; Jiang, K. A Multifunctional Flexible Tactile Sensor for Simultaneous Pressure, Temperature, and Material Recognition. *Adv. Funct. Mater.* **2025**, No. e21585.
(16) Zang, G.; Ren, J.; Shi, Y.; Peng, D.; Zheng, P.; Zheng, K.; Liu, Z.; Wang, Z.; Cheng, X.; Liu, A.-Q.; Zhu, W. Inverse Design of Aberration-Corrected Hybrid Metalenses for Large Field of View Thermal Imaging across the Entire Longwave Infrared Atmospheric Window. *ACS Nano* **2024**, *18* (49), 33653−33663.
(17) Ding, H.; Liu, K.; Zhao, X.; Su, B.; Jiang, D. Thermoelectric nanofluidics Probing Thermal Heterogeneity inside Single Cells. *J. Am. Chem. Soc.* **2023**, *145* (41), 22433−22441.
(18) Lin, M.; Zheng, Z.; Yang, L.; Luo, M.; Fu, L.; Lin, B.; Xu, C. A High-performance, Sensitive, Wearable Multifunctional Sensor Based on Rubber/CNT for Human Motion and Skin Temperature Detection. *Adv. Mater.* **2022**, *34* (1), No. 2107309.
(19) Krishnan, S. R.; Su, C.; Xie, Z.; Patel, M.; Madhvapathy, S. R.; Xu, Y.; Freudman, J.; Ng, B.; Heo, S. Y.; Wang, H.; Ray, T. R.; Leshock, J.; Stankiewicz, I.; Feng, X.; Huang, Y.; Gutruf, P.; Rogers, J. A. Wireless, Battery-free Epidermal Electronics for Continuous, Quantitative, Multimodal Thermal Characterization of Skin. *Small* **2018**, *14* (47), No. 1803192.
(20) Donner, J. S.; Thompson, S. A.; Kreuzer, M. P.; Baffou, G.; Quidant, R. Mapping Intracellular Temperature Using Green Fluorescent Protein. *Nano Lett.* **2012**, *12* (4), 2107−2111.
(21) Xu, M.; Zou, X.; Su, Q.; Yuan, W.; Cao, C.; Wang, Q.; Zhu, X.; Feng, W.; Li, F. Ratiometric Nanothermometer in Vivo Based on

Triplet Sensitized Upconversion. *Nat. Commun.* **2018**, *9* (1), No. 2698.
(22) Sun, F.; Zhou, J.; Dai, B.; Qian, T.; Zeng, J.; Li, X.; Zhuo, Y.; Zhang, Y.; Wang, Y.; Qian, C.; Tan, K.; Feng, J.; Dong, H.; Lin, D.; Cui, G.; Li, Y. Next-Generation GRAB Sensors for Monitoring Dopaminergic Activity in Vivo. *Nat. Methods* **2020**, *17* (11), 1156−1166.
(23) Kato, Y. S.; Shimazaki, Y.; Chuma, S.; Shiraya, K.; Nakane, Y.; Sugi, T.; Okabe, K.; Harada, Y.; Sotoma, S. Fluorescent Thermometers Based on Carbon Quantum Dots with Various Detection Modes for Intracellular Temperature Measurement. *Nano Lett.* **2025**, *25* (14), 5688−5696.
(24) Chen, L.; Yin, J.; Wang, Y.; Fan, Y.; Pei, Y.; Cai, Z.; Yan, W.; Hu, D.; Wang, Q.; Wang, H.; Liu, Z.; Bian, Z.; Li, F. Time-resolved Ratiometric Fluorescence Nanothermometer for Real-time Endoscopic Temperature Guidance during Tumor Ablation. *Adv. Mater.* **2025**, *37* (28), No. 2503726.
(25) Zhou, J.; Del Rosal, B.; Jaque, D.; Uchiyama, S.; Jin, D. Advances and Challenges for Fluorescence Nanothermometry. *Nat. Methods* **2020**, *17* (10), 967−980.
(26) Liu, Z.; Hou, X.; You, H.; Wang, Z.; Zhu, K.; Hu, X.; Li, P.; Lu, X.; Wang, Q.; Liu, Z.; Hu, D.; Su, J.; Dai, N.; Li, Y. Surface Copassivation Strategy for Developing Water-Soluble InP Colloidal Quantum Dots with High Luminescence and Suppressed Blinking. *J. Am. Chem. Soc.* **2025**, *147* (6), 4778−4789.
(27) Michalet, X.; Pinaud, F. F.; Bentolila, L. A.; Tsay, J. M.; Doose, S.; Li, J. J.; Sundaresan, G.; Wu, A. M.; Gambhir, S. S.; Weiss, S. Quantum Dots for Live Cells, in Vivo Imaging, and Diagnostics. *Science* **2005**, *307* (5709), 538−544.
(28) Alivisatos, A. P. Semiconductor Clusters, Nanocrystals, and Quantum Dots. *Science* **1996**, *271* (5251), 933−937.
(29) de Arquer, F. P. G.; Talapin, D. V.; Klimov, V. I.; Arakawa, Y.; Bayer, M.; Sargent, E. H. Semiconductor Quantum Dots: Technological Progress and Future Challenges. *Science* **2021**, *373* (6555), No. eaaz8541.
(30) Liu, M.; Yazdani, N.; Yarema, M.; Jansen, M.; Wood, V.; Sargent, E. H. Colloidal Quantum Dot Electronics. *Nat. Electron.* **2021**, *4* (8), 548−558.
(31) Brus, L. E. Electron−Electron and Electron-hole Interactions in Small Semiconductor Crystallites: The Size Dependence of the Lowest Excited Electronic State. *J. Chem. Phys.* **1984**, *80* (9), 4403−4409.
(32) Zhou, D.; Lin, M.; Liu, X.; Li, J.; Chen, Z.; Yao, D.; Sun, H.; Zhang, H.; Yang, B. Conducting the Temperature-Dependent Conformational Change of Macrocyclic Compounds to the Lattice Dilation of Quantum Dots for Achieving an Ultrasensitive Nanothermometer. *ACS Nano* **2013**, *7* (3), 2273−2283.
(33) Zhao, H.; Liang, H.; Vidal, F.; Rosei, F.; Vomiero, A.; Ma, D. Size Dependence of Temperature-Related Optical Properties of PbS and PbS/CdS Core/Shell Quantum Dots. *J. Phys. Chem. C* **2014**, *118* (35), 20585−20593.
(34) Ye, Z.; Lin, X.; Wang, N.; Zhou, J.; Zhu, M.; Qin, H.; Peng, X. Phonon-Assisted up-Conversion Photoluminescence of Quantum Dots. *Nat. Commun.* **2021**, *12* (1), No. 4283.
(35) Yang, J.-M.; Yang, H.; Lin, L. Quantum Dot Nano Thermometers Reveal Heterogeneous Local Thermogenesis in Living Cells. *ACS Nano* **2011**, *5* (6), 5067−5071.
(36) Adelsberger, H.; Zainos, A.; Alvarez, M.; Romo, R.; Konnerth, A. Local Domains of Motor Cortical Activity Revealed by Fiber-Optic Calcium Recordings in Behaving Nonhuman Primates. *Proc. Natl. Acad. Sci. U.S.A.* **2014**, *111* (1), 463−468.
(37) Zhang, Y.; Hu, Y.; Liu, Q.; Lou, K.; Wang, S.; Zhang, N.; Jiang, N.; Yetisen, A. K. Multiplexed Optical Fiber Sensors for Dynamic Brain Monitoring. *Matter* **2022**, *5* (11), 3947−3976.
(38) Ran, Y.; Xu, Z.; Chen, M.; Wang, W.; Wu, Y.; Cai, J.; Long, J.; Chen, Z.; Zhang, D.; Guan, B. Fiber-Optic Theranostics (FOT): Interstitial Fiber-Optic Needles for Cancer Sensing and Therapy. *Adv. Sci.* **2022**, *9* (15), No. 2200456.
(39) Jing, J.; Liu, K.; Jiang, J.; Xu, T.; Xiao, L.; Zhan, X.; Liu, T. Optimally Configured Optical Fiber Near-Field Enhanced Plasmonic Resonance Immunoprobe for the Detection of Alpha-Fetoprotein. *Adv. Sci.* **2023**, *10* (15), No. 2207437.
(40) Zheng, P.; Xiao, Y.; Xiong, P.; Su, S.; Yang, A.; Wang, X.; Xu, S.; Shao, P.; Zhou, Z.; Wu, S.; Song, E.; Gan, J.; Chen, D. Flexible Optical Fiber Stress/Temperature Dual-mode Sensing Based on CaZnOS:Nd,Er. *Adv. Funct. Mater.* **2025**, *35* (38), No. 2505094.
(41) Moon, H.; Lee, C.; Lee, W.; Kim, J.; Chae, H. Stability of Quantum Dots, Quantum Dot Films, and Quantum Dot Light-emitting Diodes for Display Applications. *Adv. Mater.* **2019**, *31* (34), No. 1804294.
(42) Wegner, K. D.; Hildebrandt, N. Quantum Dots: Bright and Versatile in Vitro and in Vivo Fluorescence Imaging Biosensors. *Chem. Soc. Rev.* **2015**, *44* (14), 4792−4834.
(43) Zeng, Y.; Ma, S.; Cao, F.; Chen, W.; Wang, Q.; Jin, G.; Wei, J.; Liu, F.; Manna, L.; Yang, X.; Li, H. High-Efficiency and Stable Colloidal One-Dimensional Core/Shell Nanorod Light-Emitting Diodes. *Nano Lett.* **2024**, *24* (18), 5647−5655.
(44) Baek, H.; Kang, S.; Heo, J.; Choi, S.; Kim, R.; Kim, K.; Ahn, N.; Yoon, Y.-G.; Lee, T.; Chang, J. B.; Lee, K. S.; Park, Y.-G.; Park, J. Insights into Structural Defect Formation in Individual InP/ZnSe/ZnS Quantum Dots under UV Oxidation. *Nat. Commun.* **2024**, *15* (1), No. 1671.
(45) Chemaly, E. R.; Troncone, L.; Lebeche, D. SERCA Control of Cell Death and Survival. *Cell Calcium* **2018**, *69*, 46−61.
(46) Yin, N.; Yu, Y.; Wang, X.; Shu, Y.; Wang, J. Dual Lanthanide Complexes-Loaded Ratiometric Nanothermometer for Elucidating Intracellular Variations of Temperature and Calcium Transport. *Chem. Eng. J.* **2024**, *490*, No. 151645.
(47) de Meis, L.; Arruda, A. P.; Carvalho, D. P. Role of Sarco/Endoplasmic Reticulum Ca^{2+}-ATPase in Thermogenesis. *Biosci. Rep.* **2005**, *25* (3−4), 181−190.

https://doi.org/10.1021/acsnano.6c06731
ACS Nano XXXX, XXX, XXX−XXX